# (α,γ) cross section measurements in the region of light p nuclei

S. J. Quinn, A. Spyrou, A. Simon, A. Battaglia, M. Bowers, B. Bucher, C. Casarella, M. Couder, P. A. DeYoung, A. C. Dombos, J. Görres, A. Kontos, Q. Li, A. Long, M. Moran, N. Paul, J. Pereira, D. Robertson, K. Smith, M. K. Smith, E. Stech, R. Talwar, W. P. Tan, and M. Wiescher

# $(\alpha,\gamma)$ cross section measurements in the region of the light p nuclei

S. J. Quinn,[1, 2, 3] A. Spyrou,[1, 2, 3, *] A. Simon,[1, 3, 4] A. Battaglia,[4] M. Bowers,[4] B. Bucher,[4] C. Casarella,[4]
M. Couder,[4] P. A. DeYoung,[5] A. C. Dombos,[1, 2, 3] J. Görres,[4] A. Kontos,[4] Q. Li,[4] A. Long,[4] M. Moran,[4] N. Paul,[4]
J. Pereira,[1] D. Robertson,[4] K. Smith,[4] M. K. Smith,[4] E. Stech,[4] R. Talwar,[4] W. P. Tan,[4] and M. Wiescher[4]

[1]*National Superconducting Cyclotron Laboratory, Michigan State University, East Lansing, MI 48824, USA*
[2]*Department of Physics & Astronomy, Michigan State University, East Lansing, MI 48824, USA*
[3]*Joint Institute for Nuclear Astrophysics, Michigan State University, East Lansing, MI 48824, USA*
[4]*Department of Physics and The Joint Institute for Nuclear Astrophysics,
University of Notre Dame, Notre Dame, IN 46556, USA*
[5]*Department of Physics, Hope College, Holland, MI 49423, USA*
(Dated: September 10, 2015)

The $^{90}$Zr$(\alpha,\gamma)^{94}$Mo, $^{92}$Zr$(\alpha,\gamma)^{96}$Mo, and $^{74}$Ge$(\alpha,\gamma)^{78}$Se reaction cross sections were measured for the first time in an effort to expand the existing experimental database for $(\alpha,\gamma)$ reactions relevant for the production of the p nuclei in the universe. In particular, the $^{90}$Zr$(\alpha,\gamma)^{94}$Mo reaction was identified by a sensitivity study for its potential impact for the $\gamma$-process mass flow in the region of the light p nuclei. The measurements were performed for energies $E_\alpha = 9.5 - 12.0$ MeV at the University of Notre Dame using the SuN detector and the $\gamma$-summing technique. The results are compared to theoretical calculations from the TALYS and NON-SMOKER nuclear reaction codes, and it is shown that the data greatly reduces the uncertainty in the cross section for the measured energies. The TALYS parameters that provide the best description of the experimental data are reported.

**PACS numbers** 24.60.Dr, 25.40.Lw, 26.30.Ef

## I. INTRODUCTION

How to accurately reproduce the observed abundances of the 35 stable, neutron-deficient isotopes from $^{74}$Se through $^{196}$Hg has remained an open question in the field of nuclear astrophysics. These "p nuclei" are shielded by the valley of stability from production via the s- and r-neutron capture processes, which create the majority of isotopes heavier than iron. Instead, the p nuclei must be produced through an alternative mechanism known as the p process [1, 2]. Presently, it is uncertain whether the p process is comprised of one astrophysical scenario or if multiple nucleosynthesis processes contribute.

In the influential B$^2$FH paper [3], the authors proposed that the p process consists of proton capture reactions on preexisting s- and r- process nuclei at high temperatures inside the hydrogen shell of a massive star when it explodes as a type II supernova (SNII). However, it was later shown that the high temperatures and densities required to produce the p nuclei in this fashion are not reached in the hydrogen shell [4]. Two alternative explosive processes involving proton captures have subsequently been identified as likely candidates for synthesizing the p nuclei, namely the $\nu$p process [5] and the rp process [6]. The site of the $\nu$p process lies in the innermost, proton-rich ejected layers of SNII, while the rp process is expected to power X-ray bursts through the burning of hydrogen and helium material accreted onto the surface of a neutron star. While the $\nu$p and rp pro-

cesses may synthesize some of the less-massive p nuclei, there is an astrophysical scenario that can produce the p nuclei across the entire mass range. This scenario consists of $(\gamma,n)$, $(\gamma,p)$, and $(\gamma,\alpha)$ photodisintegration reactions, their inverse capture reactions, and $\beta^+$ decays, whose net result is to convert existing seed nuclei into the p nuclei. The name p process remains, however this scenario is often referred to as the $\gamma$ process in the literature due to the prevalence of photodisintegration reactions. Reviews of the $\gamma$ process can be found in Refs. [1, 2].

The stellar environment necessary for the $\gamma$ process to occur is reached naturally in the O/Ne layers of SNII, and has been shown to occur in type Ia supernovae as well [7, 8]. In the O/Ne layers of SNII, peak temperatures in the range of 1.8 to 3.3 GK during the explosion allow the p nuclei to be produced without completely photodissociating the seed nuclei into the more bound nuclei in the iron region. Therefore, the $\gamma$ process in SNII has been the most studied scenario to date. Despite 25 years of work [9], models of the $\gamma$ process do not accurately reproduce the observed abundances of the p nuclei. In particular, there is a notable underproduction of the $^{92,94}$Mo and $^{96,98}$Ru isotopes by greater than a factor of 10 from the models [10]. On the other hand, the models significantly overproduce the amount of $^{74}$Se by approximately a factor of 3 [10]. Such large discrepancies in the production of the lighter p nuclei motivate the experimental investigation of reactions in this mass region.

In total, the $\gamma$ process involves hundreds of nuclei and thousands of nuclear reactions. However very little experimental data exists, for instance less than 20 of the relevant $(\alpha,\gamma)$ reactions have been measured to date [2].

_____

*spyrou@nscl.msu.edu

Due to the lack of experimental data, reaction networks of the $\gamma$ process rely heavily on theoretical reaction rates which typically have large uncertainties. To reduce the uncertainty in the production of the p nuclei through the $\gamma$ process, additional experimental data is needed. With new experimental results, the uncertainty in both the reaction rate of the measured reaction as well as the corresponding inverse reaction can be reduced. On a more global scale, experimental data can be used to put constraints on the theoretical models, which in turn can improve the predictive power for unmeasured reactions.

Due to the large number of reactions involved in the $\gamma$ process, it is not feasible to measure all of them and efforts have been made to identify a smaller list of reactions which have the largest impact on the final abundances of the p nuclei. Such sensitivity studies are valuable because they inform experimentalists which reactions are the most crucial to measure. One such sensitivity study by Rauscher [11] took the approach of identifying the isotope of each element where the $(\gamma,p)$ or $(\gamma,\alpha)$ photodisintegration rates are comparable to the $(\gamma,n)$ rates. Near stability the $(\gamma,n)$ reactions dominate, but as the isotopes become more neutron-deficient, the $(\gamma,p)$ or $(\gamma,\alpha)$ reactions may proceed with a higher rate. Accurately constraining the reaction rates at these "branching points" is critical for correctly modeling the mass flow of the $\gamma$ process. Because the location of the branching points at a given temperature rely solely on the nuclear properties, it is possible to identify potentially critical reactions independently of the astrophysical model.

In Rauscher's study [11], the branching point in the Mo isotopes was determined to be at $^{94}$Mo, at which point the $(\gamma,\alpha)$ reaction is expected to proceed at a higher rate than the $(\gamma,n)$ reaction for $\gamma$-process temperatures. However, the two reaction channels have reaction rates that are within the theoretical uncertainty of each other, which makes the identification of $^{94}$Mo as a branching point sensitive to the individual reaction rates. This is illustrated in Fig. 1, which shows JINA REACLIB reaction rates [12] for the photodissociation of $^{94}$Mo through the $(\gamma,n)$, $(\gamma,p)$, and $(\gamma,\alpha)$ channels as a function of temperature. The uncertainty in the rates was taken to be a factor of 10 for the $(\gamma,\alpha)$ reaction and a factor of 5 for the $(\gamma,n)$ and $(\gamma,p)$ reactions. Within the $\gamma$-process window of $1.8 - 3.3$ GK, the $^{94}$Mo$(\gamma,\alpha)^{90}$Zr and $^{94}$Mo$(\gamma,n)^{93}$Mo reactions are within the theoretical uncertainty of each other. If the actual $^{94}$Mo$(\gamma,\alpha)^{90}$Zr reaction rate is towards the lower end of its uncertainty band, then the $(\gamma,n)$ reaction would proceed with a higher rate, and the branching point in molybdenum would be shifted to more neutron deficient isotopes, potentially increasing the production of the isotope $^{92}$Mo. Therefore, the $^{90}$Zr$(\alpha,\gamma)^{94}$Mo was identified as one of the critical reactions to investigate experimentally to improve the understanding of the $\gamma$-process mass flow in this mass region [11].

In this paper, we report on the first measurement of the $^{90}$Zr$(\alpha,\gamma)^{94}$Mo reaction, as well as the first ever measure-
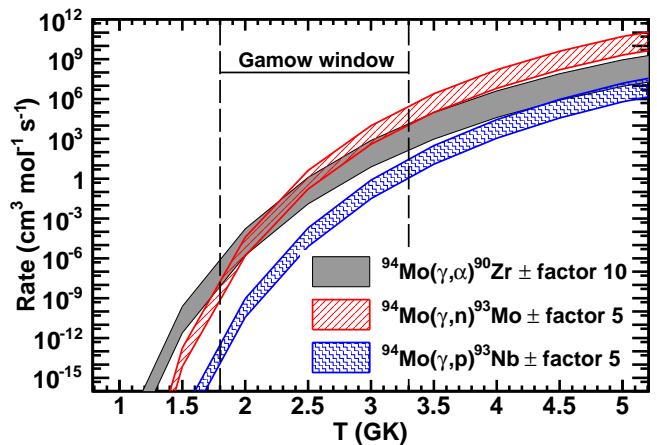


FIG. 1: (Color online) REACLIB stellar reaction rates [12] as a function of temperature for the photodissociation of $^{94}$Mo through the $(\gamma,n)$, $(\gamma,p)$, and $(\gamma,\alpha)$ channels. The width of the curves corresponds to a factor of 10 uncertainty in the $(\gamma,\alpha)$ reaction rate and a factor of 5 uncertainty in the $(\gamma,n)$ and $(\gamma,p)$ rates. Within the $\gamma$-process window of $1.8-3.3$ GK, the $^{94}$Mo$(\gamma,\alpha)^{90}$Zr reaction could have a higher rate than the $^{94}$Mo$(\gamma,n)^{93}$Mo reaction and could therefore be a branching point in the $\gamma$ process [11].

ments of the $^{92}$Zr$(\alpha,\gamma)^{96}$Mo and $^{74}$Ge$(\alpha,\gamma)^{78}$Se reactions. These three reactions are relevant for the production of the lightest p nuclei where large discrepancies between astrophysical calculations and the observed abundances are found. The uncertainties in the individual reaction cross sections are greatly reduced with the new results presented here. In addition, the measurements contribute to a larger effort aimed at constraining the reaction theory relevant to the $\gamma$ process through systematic measurements across a large mass and energy range. We discuss the details of the experiment in Sec. II, followed by the results and discussion of the individual reactions in Sec. III and IV. A summary of the paper is presented in Sec. V.

## II. EXPERIMENTAL DETAILS

The experiment was performed at the University of Notre Dame. The FN Tandem Van de Graaff accelerator was used to accelerate a $^4$He$^{2+}$ beam to energies between 9.5 to 12.0 MeV in 0.5 MeV steps. The $\alpha$ particles impinged onto isotopically-enriched targets. The beam intensity reaching the experimental endstation was monitored with a Faraday cup and charge integrator and was set in a range between $4.3 \times 10^9$ and $2.5 \times 10^{10}$ pps as needed to maximize the count rate and minimize detection dead time. The dead time was kept below 1.8% for all measurements reported here.

The $^{90}$Zr and $^{92}$Zr targets were self-supporting foils with thicknesses of 969(48) and 960(47) $\mu$g/cm$^2$, respectively, and both were isotopically enriched to 98(1)%. In

order to eliminate scattered $\alpha$ particles from hitting the beam pipe after passing through the Zr foils, a tantalum backing, or beam-stop, was placed directly behind each foil during the measurements. In the $^{74}$Ge$(\alpha,\gamma)^{78}$Se case, the $^{74}$Ge was made through the evaporation of 97.55% enriched $^{74}$Ge powder onto tantalum backing and had a thickness of 320(16) $\mu$g/cm$^2$. The thicknesses of the three targets were measured using Rutherford Backscattering Spectrometry (RBS) performed at the Hope College Ion Beam Analysis Laboratory (HIBAL) and the analysis was performed using the SIMNRA software package [13].

The nuclei produced as a result of a successful $\alpha$ capture are formed in an excited state at an energy equal to $E_{c.m.}+Q$, where $E_{c.m.}$ is the center-of-mass energy of the projectile-target system and $Q$ is the reaction $Q$ value. The $(\alpha,\gamma)$ reactions on $^{90}$Zr, $^{92}$Zr, and $^{74}$Ge reported here have $Q$ values of 2064.2, 2758.9, and 6028.4 keV, respectively. When combined with the beam energy of $E_{\alpha} = 9.5 - 12.0$ MeV, these $Q$ values produce excitation energies from approximately 11 to 17 MeV. Such high-lying excited states deexcite through many different possible $\gamma$-ray cascades, and in these experiments the emitted $\gamma$-rays were detected using the National Superconducting Cyclotron Laboratory's Summing NaI(Tl) (SuN) detector.

The SuN detector is a large-volume, cylindrical detector consisting of eight NaI segments and a total of 24 photomultiplier tubes. There is a 45 mm borehole along the axis which allows the target to be mounted at its center. Additional details on the design and characteristics of the SuN detector and its data acquisition system are contained in Ref. [14]. Due to SuN's large size and angular coverage, there is a high efficiency for detecting $\gamma$ rays emitted from the target position. By adding the energy of all $\gamma$ rays originating from a single cascade together, a "sum peak" is produced in the total $\gamma$-summed spectrum at an energy of $E_{\Sigma} = E_{c.m.} + Q$. Therefore, the number of events found in the sum peak is directly related to the number of $(\alpha,\gamma)$ reactions that took place, after taking into account the $\gamma$-summing efficiency. The $(\alpha,\gamma)$ reaction cross section is calculated by

$$\sigma = \frac{N_{\Sigma}}{N_{\alpha}\, n_t\, \varepsilon_{\Sigma}} \qquad (1)$$

where $N_{\Sigma}$ is the number of counts in the sum peak, $N_{\alpha}$ is the number of projectiles, $n_t$ is the areal target density, and $\varepsilon_{\Sigma}$ is the $\gamma$-summing efficiency. This experimental method of determining the reaction cross section is known as the $\gamma$-summing technique [14, 15].

As previously mentioned, the number of $\alpha$ particles impinging on the target was calculated based on the output of a Faraday cup and charge integrator, and the target thicknesses were determined through separate RBS measurements. Both of these quantities have approximately a 5% uncertainty. The integral of the sum peak for each measurement was taken as the number of counts above a linear background in the sum-peak region. Due to the low intensities of the $(\alpha,\gamma)$ sum peaks, the statisti-
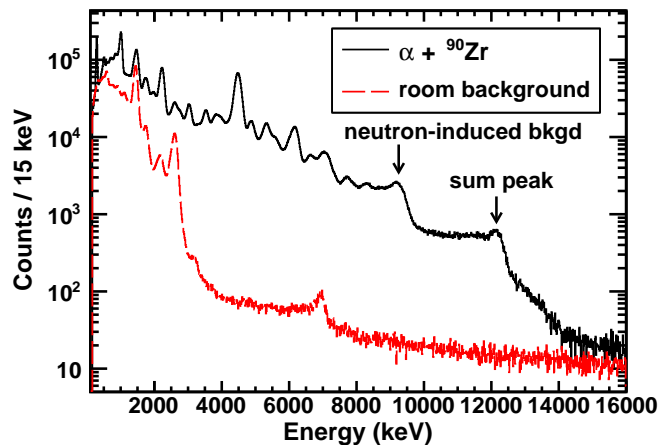


FIG. 2: *(Color online)* Total $\gamma$-summed spectrum for an $\alpha$ beam impinging onto the enriched $^{90}$Zr target at $E_{c.m.} = 9.94$ MeV, with the $^{90}$Zr$(\alpha,\gamma)^{94}$Mo sum peak at 12 MeV. The peak around 9 MeV in the spectrum comes from neutrons released in the $^{90}$Zr$(\alpha,$n$)^{93}$Mo reaction. Also plotted is the normalized room background.

cal error associated with the integrals was $6 - 14\%$. The last quantity, the $\gamma$-summing efficiency, was determined using the "hit pattern" method introduced in Ref. [14] which makes use of the segmentation of the SuN detector. When a $\gamma$-ray cascade occurs, the average number of SuN's segments that detect $\gamma$-ray energy (the hit pattern) is directly related to the average number of $\gamma$-rays emitted in the cascade. Through GEANT4 simulations of the SuN detector, the relationship between the sumpeak energy, the hit pattern, and $\gamma$-summing efficiency is well-understood. Therefore in the analysis, the experimental values of the sum-peak energy and hit pattern are compared to GEANT4 simulations to extract the efficiency. For the cross section values reported here, the $\gamma$-summing efficiency is the largest source of uncertainty with values of up to $\pm 17\%$.

### III. RESULTS

#### A. $^{90}$Zr$(\alpha,\gamma)^{94}$Mo

The $^{90}$Zr$(\alpha,\gamma)^{94}$Mo reaction was measured in the energy range of $E_{c.m.} = 9.0 - 11.4$ MeV. The total $\gamma$-summed spectrum for an energy of $E_{c.m.} = 9.94$ MeV is shown in Fig. 2 along with the normalized room-background spectrum. The majority of low energy peaks in the spectrum can be attributed to contaminants in the tantalum backing used during the measurements. At an energy of approximately 12 MeV, the sum peak of the $^{90}$Zr$(\alpha,\gamma)^{94}$Mo reaction is indicated. Also indicated is the peak around 9 MeV, which originates from neutrons released in the $^{90}$Zr$(\alpha,$n$)^{93}$Mo reaction that are captured by the NaI crystal.

TABLE I: Cross sections for the $^{90}$Zr($\alpha,\gamma$)$^{94}$Mo reaction.

| $E_{c.m.}$ (MeV) | $\sigma$ (mb) |
|---|---|
| $8.98 \pm 0.03$ | $0.060 \pm 0.018$ |
| $9.46 \pm 0.02$ | $0.093 \pm 0.024$ |
| $9.94 \pm 0.02$ | $0.155 \pm 0.028$ |
| $10.42 \pm 0.02$ | $0.171 \pm 0.028$ |
| $10.90 \pm 0.02$ | $0.207 \pm 0.034$ |
| $11.39 \pm 0.02$ | $0.307 \pm 0.051$ |

TABLE II: Cross sections for the $^{92}$Zr($\alpha,\gamma$)$^{96}$Mo reaction.

| $E_{c.m.}$ (MeV) | $\sigma$ (mb) |
|---|---|
| $9.96 \pm 0.03$ | $0.034 \pm 0.008$ |
| $10.44 \pm 0.03$ | $0.057 \pm 0.012$ |
| $10.92 \pm 0.03$ | $0.090 \pm 0.018$ |
| $11.40 \pm 0.03$ | $0.116 \pm 0.024$ |

The cross section values for the $^{90}$Zr($\alpha,\gamma$)$^{94}$Mo reaction are listed in Table I. The effective center-of-mass energy of each data point was calculated by taking into account the variation in cross section through the $^{90}$Zr target. In this calculation, the slope of the cross section was taken from the best-fit theoretical calculation to the data (see Sec. IV). The energy loss through the target was between 0.22 and 0.26 MeV for the measurements here.

### B. $^{92}$Zr($\alpha,\gamma$)$^{96}$Mo

The $^{92}$Zr($\alpha,\gamma$)$^{96}$Mo reaction was measured at energies $E_{c.m.} = 10.0 - 11.4$ MeV. Fig. 3 contains the experimental $\gamma$-summed spectrum for the measurement taken at $E_{c.m.} = 11.4$ MeV. The sum peak at 14.2 MeV is indicated on the plot, and is at an energy where the room background and beam-induced background are greatly reduced. In this case, the beam-induced background was determined by removing the $^{92}$Zr target so that the $\alpha$ beam impinged soley onto the tantalum backing. The neutron-induced signature around 12 MeV is also indicated on the plot and comes from neutrons released in the $^{92}$Zr($\alpha$,n)$^{95}$Mo reaction. The inset of Fig. 3 shows a zoomed-in view of the sum-peak region, along with the linear background used to calculate the integral of the peak. The sum peaks for the $^{92}$Zr($\alpha,\gamma$)$^{96}$Mo reaction had the lowest intensity of the three measured reactions, and therefore carry the largest statistical uncertainty of up to 14%.

The energy loss through the $^{92}$Zr target was $0.22 - 0.24$ MeV, and the small change in cross section through the target was taken into account in calculating the final energy value. To perform this effective energy calculation, the slope of the cross section was taken from the best-fit theoretical calculation (see Sec. IV). The final values for the center-of-mass energy and the cross sections are reported in Table II.
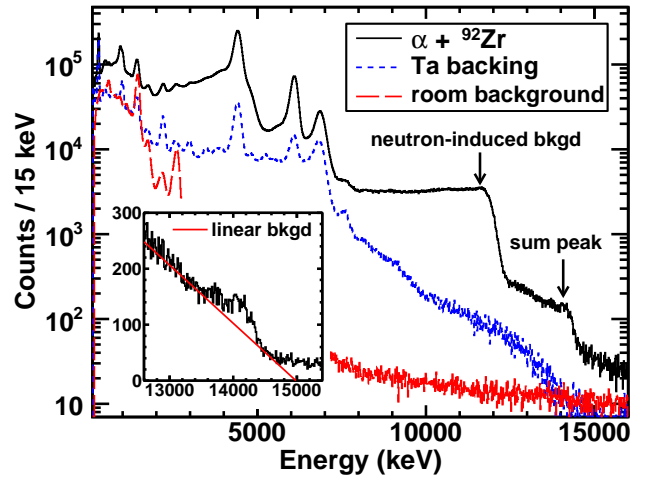


FIG. 3: *(Color online)* Total $\gamma$-summed spectrum for an $\alpha$ beam impinging onto the enriched $^{92}$Zr target at $E_{c.m.} = 11.4$ MeV, with the $^{92}$Zr($\alpha,\gamma$)$^{96}$Mo sum peak at 14.2 MeV. The peak around 12 MeV originates from neutrons emitted in the $^{92}$Zr($\alpha$,n)$^{95}$Mo reaction. Also plotted are the normalized room background and the beam-induced background from the tantalum backing. The inset shows a zoomed-in view of the sum peak and the linear background used when integrating the sum peak.

TABLE III: Cross sections for the $^{74}$Ge($\alpha,\gamma$)$^{78}$Se reaction.

| $E_{c.m.}$ (MeV) | $\sigma$ (mb) |
|---|---|
| $8.49 \pm 0.01$ | $0.048 \pm 0.008$ |
| $8.97 \pm 0.01$ | $0.075 \pm 0.012$ |
| $9.44 \pm 0.01$ | $0.080 \pm 0.014$ |
| $9.92 \pm 0.01$ | $0.113 \pm 0.021$ |
| $10.39 \pm 0.01$ | $0.124 \pm 0.026$ |
| $10.87 \pm 0.01$ | $0.169 \pm 0.039$ |

### C. $^{74}$Ge($\alpha,\gamma$)$^{78}$Se

The measurements of the $^{74}$Ge($\alpha,\gamma$)$^{78}$Se reaction were carried out for energies $E_{c.m.} = 8.5 - 10.9$ MeV. The $\gamma$-summed spectrum for the measurement at $E_{c.m.} = 8.5$ MeV is shown in Fig. 4. The sum peak at 14.5 MeV is clearly visible above the normalized room background, and the peak around 10.5 MeV comes from the effect of neutrons released in the $^{74}$Ge($\alpha$,n)$^{77}$Se reaction. After integrating the sum peak and determining the $\gamma$-summing efficiency, the cross sections were calculated with Eq. 1. The final values are reported in Table III along with the center-of-mass energy of the measurement. The energy loss through the target was $0.08 - 0.10$ MeV for the measured energies.
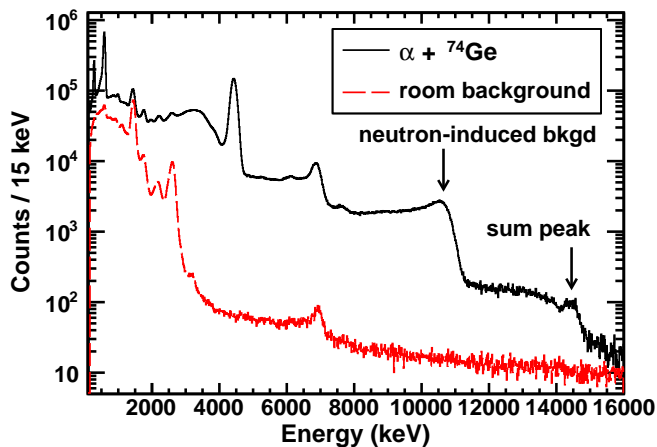
FIG. 4: *(Color online)* Total $\gamma$-summed spectrum for an $\alpha$ beam impinging onto the enriched $^{74}$Ge target at $E_{c.m.} =$ 8.5 MeV, with the $^{74}$Ge$(\alpha,\gamma)^{78}$Se sum peak at 14.5 MeV. The neutron-induced peak around 10.5 MeV comes from neutrons emitted in the $^{74}$Ge$(\alpha,n)^{77}$Se reaction. Also plotted is the normalized room background spectrum.

## IV. DISCUSSION

The experimental $(\alpha,\gamma)$ reaction cross sections contained in this paper were compared to theoretical calculations using the TALYS 1.6 nuclear reaction software package [16]. Because the states populated in the $\alpha$ capture were at high excitation energy where there are many levels that overlap, the theoretical cross sections were calculated using the nuclear statistical model. TALYS 1.6 implements Hauser-Feshbach formalism for this purpose [17], which relies on the calculation of the transmission coefficients in the entrance channel and all exit channels.

The total capture cross section is proportional to the transmission coefficient of the entrance channel, which for $\alpha$ capture reactions is calculated based on the optical model potential describing the interaction of the $\alpha$ particle and the target nucleus. The large number of nuclear levels at the $\alpha$ capture excitation energy also must be taken into account by folding in the level density with the transmission coefficient to states of each type of spin and parity. In the exit channel, the deexcitation of the produced nucleus is determined through the branching ratios of the various available reaction channels. At the energies considered here, it is possible for the deexcitation to occur through the emission of neutrons, protons, $\alpha$ particles, $\gamma$-rays, and various combinations of these particles. For the emission of nucleons, the transmission coefficients are again calculated using a nuclear optical model potential. On the other hand, the transmission coefficients for the emission of $\gamma$ rays are calculated with a $\gamma$-ray strength function. Because the deexcitation can happen to any lower energy state, it is again necessary to take into account the nuclear level density. Nuclear levels that are experimentally known are treated as discrete states instead of with a level density prescription.

Therefore, for the reactions considered here there are three ingredients that dominate the uncertainties in the theoretical cross sections; the nuclear optical model potential (OMP), the $\gamma$-ray strength function (GSF), and the nuclear level density (NLD). TALYS 1.6 has multiple options to choose from, including two OMPs for protons and neutrons, five OMPs for $\alpha$ particles, five GSFs for the dominant E1 transitions, and six NLDs. For details on all the models, the reader is directed to the TALYS 1.6 manual [18]. In the following paragraphs, only a brief description of the models with references to the original publications will be provided.

The two proton and neutron optical model potentials in TALYS are the phenomenological OMP of Koning and Delaroche [19] constrained by experimental data across a large energy and mass range (KD OMP), and the semi-microscopic OMP of Jeukenne-Lejeune-Mahaux [20] reparametrized by Bauge, Delaroche, and Girod [21] (JLM OMP). For the $\alpha$ optical model potentials, the default option in TALYS is to take the KD OMP for protons and neutrons and combine them appropriately for the $\alpha$ particle. This concept of applying OMP for single nucleons to describe interactions of more complex nuclei was first done by Watanabe for deuterons [22]. TALYS also includes the $\alpha$ potential of McFadden and Satchler [23], as well as the three potentials provided by Demetriou, Grama, and Goriely [24] which differ in their description of the imaginary part of the OMP. The first $\alpha$ potential of Demetriou et. al. used experimental data to constrain the imaginary part consisting of only a volume component, the second used a surface and volume component, and the third potential was determined using the dispersion relation to relate the imaginary part of the OMP to the real part.

The six nuclear level densities in TALYS are: the constant temperature and Fermi gas model [25, 26], the back-shifted Fermi gas model [27], the generalized superfluid model [28, 29], the microscopic level densities from Goriely's tables calculated with a Skyrme force [30], the microscopic level densities from Hilaires's table calculated with a Skyrme force [31], and the microscopic level density from Hilaire's table calculated with the Gogny interaction [32].

In TALYS, the $\gamma$-ray strength function for all transition types besides E1 are calculated with the Brink-Axel Lorentzian [33, 34]. However for the dominant E1 transitions, five different models can be used. These models are: the Kopecky-Uhl generalized Lorentzian [35], the Brink-Axel Lorentzian [33, 34], the microscopic option calculated from the Hartree-Fock BCS model [18], the microscopic option calculated from the Hartree-Fock-Bogolyubov model [18], and Goriely's hybrid model [36, 37].

In total, 300 TALYS calculations were performed for each reaction in an attempt to determine which combination of parameters best describes the data. In

TABLE IV: Ground state contribution factor X0 for the three reactions under discussion. A detailed definition of X0 can be found in Ref. [2] and the values listed in this table were taken from Ref.[40].

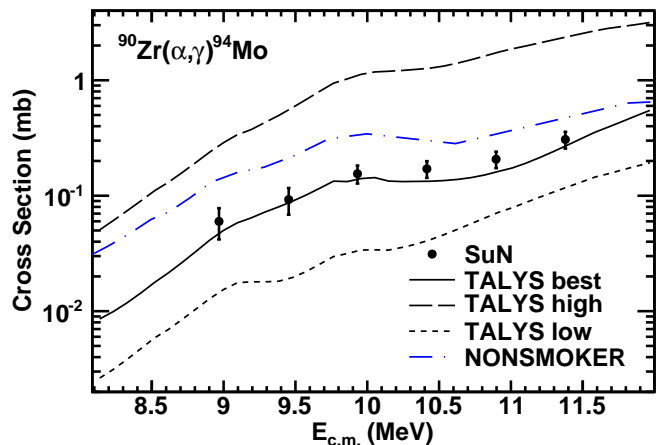| T | X0 | | |
|---|---|---|---|
| (GK) | $^{90}Zr(\alpha,\gamma)^{94}Mo$ | $^{92}Zr(\alpha,\gamma)^{96}Mo$ | $^{74}Ge(\alpha,\gamma)^{78}Se$ |
| 1.0 | 1.00 | 1.00 | 1.00 |
| 1.5 | 1.00 | 1.00 | 0.96 |
| 2.0 | 1.00 | 0.98 | 0.92 |
| 2.5 | 1.00 | 0.95 | 0.88 |
| 3.0 | 1.00 | 0.92 | 0.85 |
| 3.5 | 0.99 | 0.89 | 0.79 |
| 4.0 | 0.99 | 0.84 | 0.70 |



FIG. 5: (Color online) Experimental cross sections for the $^{90}Zr(\alpha,\gamma)^{94}Mo$ reaction compared to TALYS and NON-SMOKER calculations. The three TALYS curves correspond to the upper limit, lower limit, and best-fit calculations (see text for details).

addition to the TALYS calculations, the cross section data was also compared to Hauser-Feshbach calculations from the NON-SMOKER code obtained through the NON-SMOKER web interface [38, 39]. Since the NON-SMOKER reaction rates are used in the REACLIB database [12], they are the reaction rates that are often used in astrophysical calculations.

It is important to note that even in the astrophysical energy range, reaction rates based on laboratory measurements may not show the same sensitivity as the stellar rate. This depends on the ground state contribution X0 to the stellar rate and/or the sensitivities of the transitions from excited states in the target nucleus [2]. The cross section in the reaction direction with larger X0 is typically considered to behave similar to the stellar rate. For the three reactions studied in the present work the ground state contribution factor X0 is listed in Table IV as taken from Ref. [40] for the relevant temperatures. The values of X0 are close to one for all three reactions and therefore the laboratory measurements presented here are appropriate for constraining the stellar rate.

## A. $^{90}Zr(\alpha,\gamma)^{94}Mo$

A plot of the $^{90}Zr(\alpha,\gamma)^{94}Mo$ reaction cross sections as a function of center-of-mass energy is shown in Fig. 5. The relevant Gamow window is from 4.2 to 9.6 MeV for $\gamma$-process temperatures of $1.8 - 3.3$ GK [41]. Therefore, the data reaches the higher energies of the astrophysically relevant region and extrapolation is required for the lower energies. In addition to the data points, the result of four different theoretical calculations are shown. The upper and lower lines correspond to maximum and minimum of the TALYS calculations in this energy region, which represent the theoretical uncertainty of up to a factor of 35 for a single energy. The upper TALYS limit was calculated using the JLM OMP [20], the first Demetriou $\alpha$ potential [24], the nuclear level density from Hilaire's tables calculated with a Skyrme force [31], and the Brink-Axel Lorentzian $\gamma$-ray strength function [33, 34]. On the

other hand, the minimum TALYS limit was calculated using the KD OMP [19], the third Demetriou $\alpha$ potential [24], the nuclear level density from the constant temperature plus Fermi gas model [25, 26], and the Kopecky-Uhl generalized Lorentzian $\gamma$-ray strength function [35]. The data presented here significantly reduces the uncertainty in the $^{90}Zr(\alpha,\gamma)^{94}Mo$ reaction cross section.

Also plotted in Fig. 5 is the NON-SMOKER theoretical cross section. In the energy region plotted, the NON-SMOKER calculation overestimates the $^{90}Zr(\alpha,\gamma)^{94}Mo$ cross section by a factor of $1.6 - 2.3$, with a larger discrepancy at the lower energies. Because NON-SMOKER calculations are used in the REACLIB database, it can be concluded that the standard REACLIB reaction rate for the $^{90}Zr(\alpha,\gamma)^{94}Mo$ reaction is too high as well. In order to extract a new reaction rate, the TALYS calculation that most accurately described the data was used. In this case, the best fit was achieved with the JLM OMP [20], the second Demetriou $\alpha$ potential [24], the microscopic level densities from Hilaire's tables calculated with the Gogny force [32], and the microscopic $\gamma$-ray strength function from the Hartree-Fock BCS model [18]. The calculated reaction rates are listed in Table V. As expected, these new rates are lower than the REACLIB rate by approximately a factor of $1.9 - 2.2$ for $\gamma$-process temperatures.

In order to investigate whether the reduction in the $^{90}Zr(\alpha,\gamma)^{94}Mo$ reaction rate has an impact on the $^{94}Mo$ branching point in the $\gamma$ process, it is necessary to compare the inverse $^{94}Mo(\gamma,\alpha)^{90}Zr$ reaction rate to the $^{94}Mo(\gamma,n)^{93}Mo$ rate. The reaction rates for both reactions were taken from the REACLIB database [12] and the $^{94}Mo(\gamma,\alpha)^{90}Zr$ rate reduced by a factor of 2 as indicated by the experimental results here. Even with this reduction, the rate of photodissociating $^{94}Mo$ through

TABLE V: Stellar reaction rates for the $^{90}$Zr($\alpha,\gamma$)$^{94}$Mo reaction as calculated with TALYS1.6 [16].

| T (GK) | Rate (cm$^3$ mol$^{-1}$ s$^{-1}$) | T (GK) | Rate (cm$^3$ mol$^{-1}$ s$^{-1}$) |
|---|---|---|---|
| 0.4 | $6.385 \times 10^{-42}$ | 3.0 | $2.577 \times 10^{-7}$ |
| 0.5 | $2.962 \times 10^{-36}$ | 3.5 | $8.368 \times 10^{-6}$ |
| 0.6 | $2.955 \times 10^{-32}$ | 4.0 | $1.235 \times 10^{-4}$ |
| 0.7 | $3.762 \times 10^{-29}$ | 5.0 | $5.527 \times 10^{-3}$ |
| 0.8 | $1.374 \times 10^{-26}$ | 6.0 | $5.880 \times 10^{-2}$ |
| 0.9 | $2.189 \times 10^{-24}$ | 7.0 | $2.429 \times 10^{-1}$ |
| 1.0 | $1.867 \times 10^{-22}$ | 8.0 | $6.254 \times 10^{-1}$ |
| 1.5 | $8.485 \times 10^{-16}$ | 9.0 | $1.359 \times 10^{0}$ |
| 2.0 | $5.908 \times 10^{-12}$ | 10.0 | $2.760 \times 10^{0}$ |
| 2.5 | $2.662 \times 10^{-9}$ | | |



FIG. 6: (Color online) Experimental cross sections for the $^{92}$Zr($\alpha,\gamma$)$^{96}$Mo reaction compared to TALYS and NON-SMOKER calculations. The three TALYS curves correspond to the upper limit, lower limit, and best-fit calculations (see text for details).

the ($\gamma,\alpha$) channel is still larger than the ($\gamma$,n) channel for temperatures below 2.5 GK. Therefore, $^{94}$Mo appears to be the branching point in the molybdenum isotopic chain for temperatures below 2.5 GK. However, this could change if a future measurement of the $^{93}$Mo(n,$\gamma$)$^{94}$Mo reaction indicates that the rate is much higher than the current theoretical predictions.

### B. $^{92}$Zr($\alpha,\gamma$)$^{96}$Mo

The cross sections of the $^{92}$Zr($\alpha,\gamma$)$^{96}$Mo reaction are plotted in Fig. 6. The Gamow window is from 4.2 to 9.6 MeV for $\gamma$-process temperatures [41], so the data reaches to just above the astrophysically relevant region. Also plotted in Fig. 6 are the results from theoretical calculations with the TALYS and NON-SMOKER codes. In the energy region plotted, NON-SMOKER describes the energy dependence of the cross section well, but overestimates the values by a factor of $1.5 - 1.7$.

The three TALYS calculations that are plotted represent the upper limit, lower limit, and best description of the experimental results. The large spread between the maximum and minimum TALYS calculations show the total theoretical uncertainty of a factor of 6 at the highest energies and a factor of 29 at the lowest energies plotted. To achieve the upper limit, TALYS calculations were performed with the JLM OMP [20], the first Demetriou $\alpha$ potential [24], the nuclear level density from Hilaire's tables calculated with a Skyrme force [31], and the Brink-Axel Lorentzian $\gamma$-ray strength function [33, 34]. On the other hand, the lower TALYS limit was calculated using the KD OMP [19], the second Demetriou $\alpha$ potential [24], the nuclear level density from the constant temperature plus Fermi gas model [25, 26], and the Kopecky-Uhl generalized Lorentzian $\gamma$-ray strength function [35]. The experimental data greatly reduces the uncertainty in the cross section of the $^{92}$Zr($\alpha,\gamma$)$^{96}$Mo reaction to approximately 20%. Lastly, the TALYS calculation which most accurately describes the data was performed with the JLM OMP [20], the first Demetriou $\alpha$ potential [24], the
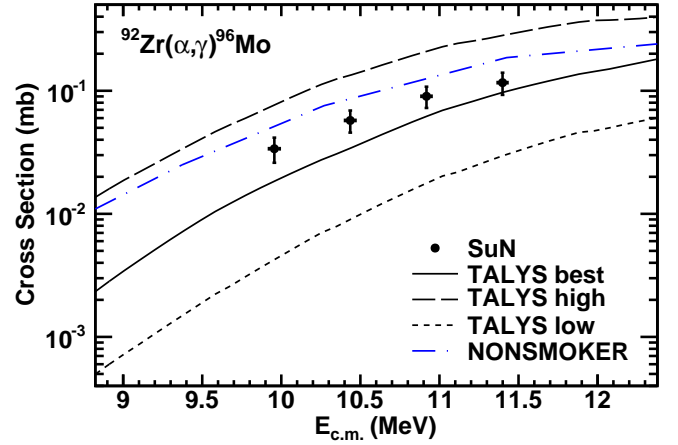
generalized superfluid level density model [28, 29], and Goriely's hybrid $\gamma$-ray strength function [36].

### C. $^{74}$Ge($\alpha,\gamma$)$^{78}$Se

A plot of the $^{74}$Ge($\alpha,\gamma$)$^{78}$Se cross section results compared to the TALYS and NON-SMOKER theoretical calculations is shown in Fig. 7. As in the case of the $^{90,92}$Zr($\alpha,\gamma$)$^{94,96}$Mo reactions, the experimental data is lower than the NON-SMOKER calculations. Here, NON-SMOKER is a factor of $1.6-2.3$ larger. The Gamow window for the $^{74}$Ge($\alpha,\gamma$)$^{78}$Se reaction is $3.5-8.4$ MeV [41] for $\gamma$-process temperatures, so the data reaches to just above the astrophysically relevant region.

The upper TALYS limit corresponds to calculations with the JLM OMP [20], the default $\alpha$ potential [18], the nuclear level density from Hilaire's tables calculated with a Skyrme force [31], and the Brink-Axel Lorentzian $\gamma$-ray strength function [33, 34]. The lower TALYS limit corresponds to calculations with the KD OMP [19], the second Demetriou $\alpha$ potential [24], the nuclear level density from Hilaire's tables calculated with the Gogny force [32], and the Kopecky-Uhl generalized Lorentzian $\gamma$-ray strength function [35]. The total theoretical uncertainty between the upper and lower bounds is a factor of 11 at the higher energies and a factor of 21 at the lower energies plotted. The experimental uncertainty of $16-23\%$ greatly constrains the cross section values in this energy region.

The experimental data was compared to the 300 TALYS calculations to determine what combination of input parameters provided the best match. The best fit to the data was achieved with TALYS calculations performed with the KD OMP [19], the default $\alpha$ potential [18], the nuclear level densities from Goriely's ta-
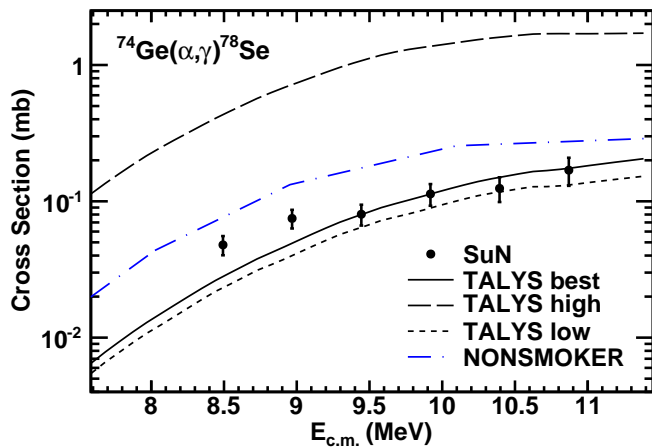
FIG. 7: (Color online) Experimental cross sections for the $^{74}$Ge($\alpha,\gamma$)$^{78}$Se reaction compared to TALYS and NON-SMOKER calculations. The three TALYS curves correspond to the upper limit, lower limit, and best-fit calculations (see text for details).

bles [30], and the microscopic $\gamma$-ray strength function calculated from the Hartree-Fock-Bogolyubov model [18].

## V.  CONCLUSIONS

In an effort to expand the very limited quantity of existing experimental data for ($\alpha,\gamma$) reactions relevant in the astrophysical $\gamma$ process, the first ever measurements of the $^{90}$Zr($\alpha,\gamma$)$^{94}$Mo, $^{92}$Zr($\alpha,\gamma$)$^{96}$Mo, and $^{74}$Ge($\alpha,\gamma$)$^{78}$Se reaction cross sections were performed by implementing the $\gamma$-summing technique with the SuN detector at the University of Notre Dame. The measurements greatly reduce the uncertainty of the cross section values between energies of $E_\alpha = 9.5 - 12.0$ MeV from a theoretical uncertainty of larger than a factor of 10 to an experimental uncertainty of approximately 20%. The nuclear reaction code TALYS was used to calculate theoretical cross sections to determine which input parameters provided the most accurate description of the data. The results of the $^{90}$Zr($\alpha,\gamma$)$^{94}$Mo reaction indicate that $^{94}$Mo is a branching point in the $\gamma$ process for temperatures below 2.5 GK.

[1] M. Arnould and S. Goriely, Phys. Rep. **384**, 1 (2003).
[2] T. Rauscher, N. Dauphas, I. Dillmann, C. Fröhlich, Z. Fülöp, and G. Gyürky, Rep. Prog. Phys. **76**, 066201 (2013).
[3] K. M. Burbidge, G. R. Burbidge, W. A. Fowler, and F. Hoyle, Rev. Mod. Phys. **29**, 547 (1957).
[4] J. Audouze and J. W. Truran, Astrophys. J. **202**, 204 (1975).
[5] C. Fröhlich, G. Martínez-Pinedo, M. Liebendörfer, F. K. Thielemann, E. Bravo, W. R. Hix, K. Langanke, and N. T. Zinner, Phys. Rev. Lett. **96**, 142502 (2006).
[6] R. K. Wallace and S. E. Woosley, Astrophys. J. Supp. Ser. **45**, 389 (1981).
[7] W. M. Howard, B. S. Meyer, and S. E. Woosley, Astrophys. J. **373**, L5 (1991).
[8] C. Travaglio, F. K. Röpke, R. Gallino, and W. Hillebrandt, Astrophys. J. **739**, 93 (2011).
[9] M. Rayet, N. Prantzos, and M. Arnould, Astron. Astrophys. **227**, 271 (1990).
[10] W. Rapp, J. Görres, M. Wiescher, H. Schatz, and F. Käppeler, Astrophys. J. **653**, 474 (2006).
[11] T. Rauscher, Phys. Rev. C **73**, 015804 (2006).
[12] R. H. Cyburt, A. M. Amthor, R. Ferguson, Z. Meisel, K. Smith, S. Warren, A. Heger, R. D. Hoffman, T. Rauscher, A. Sakharuk, et al., Astrophys. J. Supp.

Ser. **189**, 240 (2010), URL http://stacks.iop.org/0067-0049/189/i=1/a=240.
[13] M. Mayer, *SIMNRA User's Guide*, Report IPP 9/113, Max-Planck-Institut für Plasmaphysik, Garching, Germany, 1997.
[14] A. Simon, S. Quinn, A. Spyrou, A. Battaglia, I. Beskin, A. Best, B. Bucher, M. Couder, P. DeYoung, X. Fang, et al., Nucl. Instr. Meth. A **703**, 16 (2013), ISSN 0168-9002, URL http://www.sciencedirect.com/science/article/pii/S0168900212013824.
[15] A. Spyrou, H.-W. Becker, A. Lagoyannis, S. Harissopulos, and C. Rolfs, Phys. Rev. C **76**, 015802 (2007), URL http://link.aps.org/doi/10.1103/PhysRevC.76.015802.
[16] A. J. Koning, S. Hilaire, and M. C. Duijvestijn, "TALYS-1.0" *Proceedings of the International Conference on Nuclear Data for Science and Technology*, April 22-27, Nice, France, editors O. Bersillon and F. Gunsing and E. Bauge and R. Jacqmin and S. Leray and EDP Sciences, p 211-214 (2008).
[17] W. Hauser and H. Feshbach, Phys. Rev. **87**, 366 (1952), URL http://link.aps.org/doi/10.1103/PhysRev.87.366.
[18] A. Koning, S. Hilaire, and S. Goriely, *TALYS 1.6 a nuclear reaction program: User Manual*, Nuclear Research

and Consultancy Group, Westerduinweg 3, P.O. Box 25, NL-1755 ZG, Petten, The Netherlands (2013).

[19] A. Koning and J. Delaroche, Nucl. Phys. A **713**, 231 (2003), URL http://www.sciencedirect.com/science/article/pii/S0375947402013210.

[20] J. P. Jeukenne, A. Lejeune, and C. Mahaux, Phys. Rev. C **15**, 10 (1977), URL http://link.aps.org/doi/10.1103/PhysRevC.15.10.

[21] E. Bauge, J. P. Delaroche, and M. Girod, Phys. Rev. C **63**, 024607 (2001), URL http://link.aps.org/doi/10.1103/PhysRevC.63.024607.

[22] S. Watanabe, Nucl. Phys. **8**, 484 (1958), URL http://www.sciencedirect.com/science/article/pii/0029558258901809.

[23] L. McFadden and G. R. Satchler, Nucl. Phys. **84**, 177 (1966), URL http://www.sciencedirect.com/science/article/pii/002955826690441X.

[24] P. Demetriou, C. Grama, and S. Goriely, Nucl. Phys. A **707**, 253 (2002), URL http://www.sciencedirect.com/science/article/pii/S037594740200756X.

[25] A. Gilbert, F. S. Chen, and A. G. W. Cameron, Can. J. Phys. **43**, 1248 (1965), URL http://dx.doi.org/10.1139/p65-120.

[26] A. Gilbert and A. G. W. Cameron, Can. J. Phys. **43**, 1446 (1965), URL http://dx.doi.org/10.1139/p65-139.

[27] W. Dilg, W. Schantl, H. Vonach, and M. Uhl, Nucl. Phys. A **217**, 269 (1973), URL http://www.sciencedirect.com/science/article/pii/0375947473901966.

[28] A. V. Ignatyuk, K. K. Istekov, and G. N. Smirenkin, Sov. J. Nucl. Phys. **29**, 450 (1979).

[29] A. V. Ignatyuk, J. L. Weil, S. Raman, and S. Kahane, Phys. Rev. C **47**, 1504 (1993), URL http://link.aps.org/doi/10.1103/PhysRevC.47.1504.

[30] S. Goriely, F. Tondeur, and J. M. Pearson, Atom. Data Nucl. Data Tables **77**, 311 (2001), URL http://www.sciencedirect.com/science/article/pii/S0092640X0090857X.

[31] S. Goriely, S. Hilaire, and A. J. Koning, Phys. Rev. C **78**, 064307 (2008), URL http://link.aps.org/doi/10.1103/PhysRevC.78.064307.

[32] S. Hilaire, M. Girod, S. Goriely, and A. J. Koning, Phys. Rev. C **86**, 064317 (2012), URL http://link.aps.org/doi/10.1103/PhysRevC.86.064317.

[33] D. M. Brink, Nucl. Phys. **4**, 215 (1957), URL http://www.sciencedirect.com/science/article/pii/0029558287900216.

[34] P. Axel, Phys. Rev. **126**, 671 (1962), URL http://link.aps.org/doi/10.1103/PhysRev.126.671.

[35] J. Kopecky and M. Uhl, Phys. Rev. C **41**, 1941 (1990), URL http://link.aps.org/doi/10.1103/PhysRevC.41.1941.

[36] S. Goriely, Phys. Lett. B **436**, 10 (1998), URL http://www.sciencedirect.com/science/article/pii/S0370269398009071.

[37] R. Capote, M. Herman, P. Oblozinsky, P. G. Young, S. Goriely, T. Belgya, A. V. Ignatyuk, A. J. Koning, S. Hilaire, V. A. Plujko, et al., Nucl. Data Sheets **110**, 3107 (2009), URL http://www.sciencedirect.com/science/article/pii/S0090375209000994.

[38] T. Rauscher and F. K. Thielemann, At. Data Nucl. Data Tables **79**, 47 (2001), URL http://www.sciencedirect.com/science/article/pii/S0092640X01908630.

[39] T. Rauscher, *Non-smoker database* (2015), nucastro.org/nonsmoker.html, URL http://nucastro.org/nonsmoker.html.

[40] T. Rauscher, Astrophys. J. Suppl. Ser. **201**, 26 (2012).

[41] Kadonis, *Karlsruhe astrophysical database of nucleosynthesis in stars* (2015), www.kadonis.org/pprocess/gamow.php, URL www.kadonis.org/pprocess/gamow.php.